2009-01-0838

Development and Validation of a Primary Breakup Model for Diesel Engine Applications

S. Som, A.I. Ramirez, S.K. Aggarwal
University of Illinois at Chicago

A.L. Kastengren, E. El-Hannouny, D.E. Longman, C.F. Powell
Argonne National Laboratory

P.K. Senecal
Convergent Science, Inc.

Copyright © 2009 SAE International

ABSTRACT

Fuel injection characteristics, in particular the atomization and penetration of the fuel droplets in the region close to the nozzle orifice, are known to affect emission and particulate formation in Diesel engines. It is also well established that the primary fuel atomization process is induced by aerodynamics in the near nozzle region as well as cavitation and turbulence from the injector nozzle. Typical breakup models in the literature however, do not consider the effects of cavitation and turbulence from nozzle injector. In this paper, a comprehensive primary breakup model incorporating the inner nozzle flow effects such as cavitation and turbulence along with aerodynamically induced breakup is developed and incorporated in the CONVERGE CFD code. This new primary breakup model is tested in a constant volume spray chamber against various spray data available in the literature. Both evaporating and non-evaporating spray conditions are investigated since a non-evaporating spray provides a more stringent test for spray models, while evaporating spray represents a more realistic engine environment. X-ray data obtained from the Advanced Photon Source is used for a detailed validation of this primary breakup model, especially in the region close to the nozzle under non-evaporating conditions. Specifically, spray cone-angle, liquid penetration, transverse mass distribution, and normalized spray axial velocity are matched. Robust validation is performed under evaporating conditions against liquid length, and penetration data. Very good agreement is observed under all the conditions attesting the new primary breakup model's capability to capture the primary breakup phenomenon effectively.

INTRODUCTION

High-speed fuel injection in Diesel engine combustion chambers represents one of the most challenging and hence most extensively studied multiphase flow phenomena. A fundamental understanding of the breakup and atomization of the fuel jet is essential for enhancing the engine combustion efficiency and emission characteristics. In the wake of increasingly strict emission regulations (U.S. Environmental Protection Agency) and limited fossil fuel availability, it is imminent that such fundamental understanding is achieved. The atomization of a high-pressure liquid fuel jet in a Diesel engine is governed by the cavitation and turbulence processes inside the injector nozzle, followed by the aerodynamically induced instabilities outside the nozzle. Due to the radial turbulent velocity fluctuations at the surface of the jet the turbulent eddies from the nozzle can overcome the surface tension forces and thus cause disintegration of the jet.

The Engineering Meetings Board has approved this paper for publication. It has successfully completed SAE's peer review process under the supervision of the session organizer. This process requires a minimum of three (3) reviews by industry experts.
All rights reserved. No part of this publication may be reproduced, stored in a retrieval system, or transmitted, in any form or by any means, electronic, mechanical, photocopying, recording, or otherwise, without the prior written permission of SAE.
ISSN 0148-7191
Positions and opinions advanced in this paper are those of the author(s) and not necessarily those of SAE. The author is solely responsible for the content of the paper.
SAE Customer Service: Tel: 877-606-7323 (inside USA and Canada)
Tel: 724-776-4970 (outside USA)
Fax: 724-776-0790
Email: CustomerService@sae.org
SAE Web Address: http://www.sae.org

Printed in USA

Cavitation structures developed inside the nozzle orifice can reach the exit and implode, and thus cause jet disintegration. These cavitation induced disturbances have been shown to have a strong effect on the structure of the liquid spray at the nozzle exit, leading to a fragmented liquid core at the nozzle exit. Yue et al. [1] used the X-ray absorption technique and demonstrated the formation of a fragmented liquid core in the near-nozzle region. The aerodynamic break-up of the liquid jet (or fragmented liquid) outside the nozzle is caused by the growth of instabilities occurring at the liquid-gas interphase [2].

The atomization models that are currently used to simulate liquid break-up in Diesel engines can be classified into two broad categories. The first is based on the idea that the breakup is caused by the Kelvin-Helmhotlz and/or Rayleigh-Taylor instability. The Rayleigh-Taylor instability is caused by the inertia of the denser fluid when the system experiences an acceleration transverse to the interface in the direction of the denser fluid [3], while the Kelvin-Helmholtz instability is a consequence of disturbances of the relative motion between the two phases [4]. The second group of models is based on the observation that the cavitation-induced disturbances inside the nozzle lead to a fragmented liquid core at the nozzle exit. This has led to the development of models such as TAB (Taylor Analogy Break-up) [5], ETAB (Enhanced Taylor Analogy Break-up) [6], and CAB (Cascade Atomization and Drop break-up) [7] models. The basis of these TAB-based models is a droplet distortion parameter that is governed by a forced, damped, simple harmonic oscillator. When the distortion parameter reaches unity, the drop breakup occurs, and the newly formed droplets are assumed to belong to the same drop parcel that now contains smaller droplets, but the number of droplets is increased accordingly [7].

Our literature review indicates that the existing atomization and breakup models are phenomological in nature and do not take into account the nozzle flow dynamics, especially the effects of cavitation and turbulence at the nozzle exit. Arcoumanis and Gavaises [8] developed a primary breakup model accounting for the effect of collapse of cavitation bubbles at the nozzle exit. The amount of cavitation at the nozzle exit was captured using a 1-D nozzle flow model. Subsequently, they developed a more robust cavitation model [9]. However, static/dynamic linking of this robust cavitation model with spray simulations was not reported. Huh and Gosman [10] developed a phenomological breakup model considering the effects of turbulence induced instabilities. Bianchi and Pelloni [11] applied this model for spray calculations by accounting for the amount of turbulence at the nozzle exit using simple force balance. Berg et al. [12] developed a primary breakup model incorporating the effects of turbulence and cavitation. They also dynamically coupled the inner nozzle and spray simulations. While all the above models have been tested under some conditions, the ability to capture even qualitative spray characteristics with varying degree of cavitation and turbulence has not been established.

A recent study by Som and Aggarwal [13] identified the scope of improvements for current state-of-the-art breakup model. It was observed that due to the absence of a primary breakup model accounting for all the three effects (aerodynamics, turbulence, and cavitation), some experimental trends observed with nozzle orifice geometry changes could not be captured. Validation against the x-ray radiography data and optical spray measurements revealed certain short-comings of the models. While the macroscopic spray characteristics were well predicted by current spray models, spray dispersion, or spreading, was underpredicted. These inadequacies of the current breakup models form the major motivation for the present work.

The present study has two main objectives. The first is to develop and implement a primary breakup model incorporating the effects of cavitation, turbulence, and aerodynamic breakup. Static coupling between inner nozzle flow simulations [14] and the primary breakup model is also incorporated in order to characterize the effects of nozzle orifice geometry on spray development and observe if this primary breakup model can capture experimentally observed trends [15,16]. To the best of our knowledge this presents the first numerical effort examining the effect of orifice conicity and inlet radius of curvature on the spray behavior. Our eventual goal is to dynamically couple this primary breakup model and inner nozzle flows. The present work is a step towards that goal.

The second objective is to perform a comprehensive validation of the new primary breakup model for both non-evaporating and evaporating sprays. From a modeling perspective, non-evaporating sprays provide a more stringent test for spray models, especially for atomization and collision models, than evaporating sprays. Under evaporating conditions, droplets vaporize after a few time steps, while, under non-evaporating conditions, these droplets continue to undergo collision and break up, thus testing the spray sub-models to a greater degree. The recent x-ray data from ANL (Argonne National Laboratories) for non-evaporating sprays obtained under Diesel like conditions [21] has been used for testing the spray models. Such data is particularly useful, since the x-ray technique can provide the details of the spray including liquid mass distribution near the nozzle, which can not be captured by optical techniques. For evaporating sprays, we have used the well known Siebers data set [19,20]. Some of this data has not been reported in previous validation studies. Simulations have been performed using a commercial code “CONVERGE” [17,18], since it incorporates state-of-the-art spray models under Diesel engine conditions.

OVERVIEW OF EVAPORATING AND NON-EVAPORATING SPRAY EXPERIMENTS

This section provides a brief overview of evaporating spray experiments conducted at Sandia National Laboratories [19,20] using optical measurement techniques, and non-evaporating spray experiments

performed at ANL [21] using the x-ray radiography technique.

The X-ray measurements of non-evaporating sprays were performed at the Advanced Photon Source (APS) at ANL, which generates a highly intense x-ray beam with a narrow range (2% bandwidth) of x-ray wavelengths. Optical techniques are not capable of capturing any quantitative data in the optically dense region near the injector. Small droplets of the fuel spray scatter visible light, thus limiting the capabilities of optical measurements. The main interaction between the fuel and the x-rays is absorption, hence making it an appealing alternative for spray studies. Also, the x-ray absorption measurements provide information of the spray structure especially near the nozzle where the highly dense fuel region is impenetrable by optical means. This x-ray radiography technique has been used extensively to analyze the spray characteristics for single-hole research nozzles [22,23] injecting into chamber back pressure lower than typical of Diesel engines. In a recent study Ramírez et al. [21] characterized a single plume from a full production multi-hole nozzle under engine like ambient densities using x-ray radiography. This data set is used for extensive spray model validations and parametric studies. A summary of the test conditions is provided in Table 1.

Parameter	Quantity
Injection System	Caterpillar HEUI 315B
Number of Orifices	6
Orifice Diameter [μm]	169 with L/D = 4.412
Oil Rail Pressure [MPa]	Case 1: 17 | Case 2: 21
Pressure Intensification ratio	6.6
Fill Gas	Nitrogen (N_2)
Chamber Density [kg/m^3]	34.13
Fuel	Viscor & Cerium blend
Fuel Density [kg/m^3]	865.4
Fuel Temperature [°C]	40
Fuel Injection Quantity [mm^3/stroke]	100
Calculated discharge Coefficient	Case 1: 0.82 | Case 2: 0.81

Table 1. Test Conditions for non-evaporating spray experiments [21].

ROI measurements reported by Ramirez et al. [21] for the HEUI system are for a combination of all six orifices. This measured ROI from the Bosch rate meter led to gross underprediction of spray penetration [21]. Hence the initial ROI obtained from x-ray data was combined with the steady state ROI measured from the Bosch meter to construct an injection rate for the duration of injection. The total mass injected through the single hole of the nozzle was one-sixth of the total mass injected. The hybrid ROI profile used in the numerical model is shown in Figure 1. The regions obtained from x-ray and rate meter are indicated on the plot.

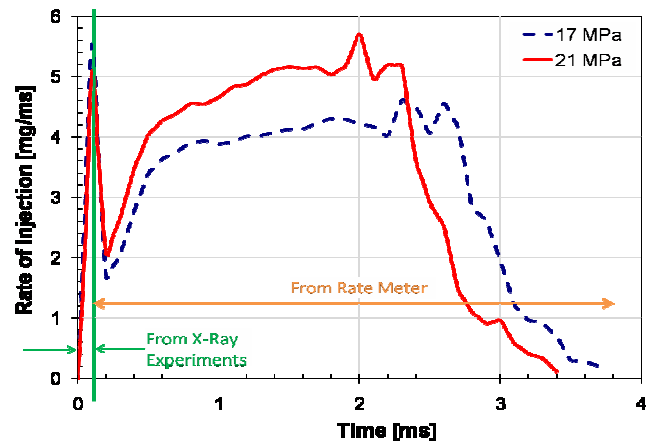

Figure 1: Hybrid ROI profile of a single orifice used for input in numerical simulation.

Siebers [19] conducted evaporating spray experiments under diesel like conditions in a quiescent constant volume chamber. The objective was to determine the sensitivity of liquid phase fuel penetration to variations in injection pressure, orifice diameter, ambient gas conditions, fuel volatility and fuel injection temperature. Summary of the test conditions is provided in Table 1. Inert conditions inside the chamber facilitated accurate measurement of penetration and vaporization of the liquid phase using optical techniques. Liquid length and vapor penetration was used for spray model validations. Rate of injection (ROI) measurements revealed a top hat injection profile which was used as an inlet boundary condition for spray calculations.

Injection System	Detroit Diesel, Common Rail
Number of Orifices	1
Orifice Diameter	100 to 500 μm L/D = 4.2
Injection Pressure [bar]	400 to 1500
Fill Gas	Mixture of N_2, H_2, O_2,C_2H_2
Chamber Density [kg/m^3]	3.3 to 60
Chamber Temperature [°K]	700 to 1300
Fuel Temperature [°K]	375 to 440
Measured discharge Coefficient	0.78 to 0.84

Table 2. Test conditions for evaporating spray experiments [19].

SPRAY MODELING SET-UP

CONVERGE incorporates state-of-the-art models for spray injection, atomization and breakup, turbulence, droplet collision and coalescence, ignition, combustion, and emissions processes. While all the details can be found elsewhere [17,18], a short description of the primary breakup KH (Kelvin-Helmholtz) model is provided.

SPRAY MODELS: The blob injection model injects liquid drops with a diameter equal to an effective nozzle diameter and the KH (Kelvin-Helmholtz) and RT (Rayleigh-Taylor) instabilities are incorporated to predict the subsequent droplet breakup. The KH model considers breakup resulting from unstable waves growing at the liquid surface [4]. Due to the relative velocity between the gas and liquid phases, the growth of KH instabilities induces the shearing of the droplets from the liquid surface. The breakup of droplet parcels is calculated by assuming that the radius of newly formed droplets (r_{KH}) is proportional to the wavelength of the fastest growing unstable surface wave on the parent droplet i.e.,

$$r_{KH} = B_0 \Lambda_{KH} \quad (1)$$

During breakup, the radius of the parent droplet parcel (r) decreases continuously according to the following equation until it reaches the stable droplet radius (r_{KH}):

$$\frac{dr}{dt} = \frac{r - r_{KH}}{\tau_{KH}}, \; r_{KH} \le r \quad (2)$$

$$\tau_{KH} = \frac{3.276 B_1 r}{\Omega_{KH} \Lambda_{KH}} \quad (3)$$

Here Ω_{KH} and Λ_{KH} are given by Eqs. 4 and 5 respectively and B_1 is the KH time constant. The frequency of the fastest growing wave and its corresponding wavelength are given by:

$$\Omega_{KH} = \frac{0.34 + 0.38 We_g^{1.5}}{(1+Z)\left(1+1.4T^{0.6}\right)} \sqrt{\frac{\sigma}{\rho_l r^3}} \quad (4)$$

$$\Lambda_{KH} = \frac{9.02 r \left(1+0.45\sqrt{Z}\right)\left(1+0.4T^{0.7}\right)}{\left(1+0.865 We_g^{1.67}\right)^{0.6}} \quad (5)$$

where, $Z\ (Ohnesorge\ number) = \dfrac{\sqrt{We_l}}{\mathrm{Re}_l}$ (6)

$$We_l (Weber\ Number) = \frac{\rho_l U_r^2 r}{\sigma}, \mathrm{Re}_l (\mathrm{Re}\,ynolds\ Number) = \frac{U_r r}{\nu_l}$$

$$T(Taylor\ Number) = Z\sqrt{We_g}, We_g (Weber\ Number) = \frac{\rho_g U_r^2 r}{\sigma}$$

Mass is accumulated from the parent droplet until the shed mass is equal to 5% of the initial parcel mass. At this time a new parcel is created with a radius given by Eq. (1). Except for the radius, number of drops and velocity, the new parcel is given the same properties as the parent parcel. The new parcel is given a component of velocity randomly selected in the plane orthogonal to the direction of the parent parcel as:

$$v_n = C_1 \Omega_{KH} \Lambda_{KH} \quad (7)$$

The momentum of the parent parcel is adjusted so that momentum is conserved. The velocity magnitude of the new parcel is the same as the parent parcel. These child droplets undergo secondary breakup due to the competing effects of KH and RT models.

Droplet collisions are based on the NTC (No Time Counter) algorithm [24]. In the O'Rourke collision model [25] the computation cost scales with the square of the number of parcels injected (N_p), while it scales linearly with N_p in the NTC collision model. Once collision occurs, the outcomes of the collision are predicted as bouncing stretching, reflexive separation, or coalescence [26]. A single component droplet evaporation model [25] based on the Frossling correlation is used. A dynamic drag model is used which postulates that the drag coefficient is highly dependent on the shape of the droplet. An initially spherical droplet distorts significantly when the Weber number is large. The shape can vary between a sphere and a disk. The drag coefficient for a disc is significantly higher than that for a sphere. This dynamic drop model accounts for the effects of drop distortion, linearly varying between the drag of a sphere and a disk [27]. The effects of turbulence on the droplet is included using a standard turbulent dispersion model [25].

Post-processing tools were developed and implemented in CONVERGE to obtain results which can be directly compared with the line-of-sight measurements from x-ray data. All the droplets at a given time in the spray were projected to a two dimensional plane. These droplets were then accounted for based on their axial and transverse location to obtain transverse distributions of projected density, normalized spray axial velocity etc.

GRID GENERATION: CONVERGE uses an innovative modified cut-cell Cartesian method for grid generation [17,18]. The grid is generated internally to the code at runtime. For all the cases the base grid size was fixed to 4mm. In order to resolve the flow near the injector, a fixed grid embedding was employed such that the minimum grid size was 0.5mm. Apart from this region, it is rather difficult to determine where a refined grid is desired. Hence three levels of adaptive mesh refinement were employed for the velocity field such that the minimum grid size was 0.5mm. In order to match the spray chamber geometry, a cylindrical geometry of 100mm in diameter and 100mm in length was generated for evaporating sprays. For the non-evaporating sprays, a cylindrical geometry of 50mm in diameter and 200mm in length was generated. With the above mentioned grid sizes the run times were about 25-30 hours for both evaporating and non-evaporating sprays on a 4-node Linux clusters with 2.8 GHz processors.

IMPROVED KH BREAKUP MODEL: The correlations for frequency of the fastest growing wave and its corresponding wavelength were derived for $We_g \le 1000$ by Reitz [4]. At low Ohnesorge and Weber numbers the existing correlations (Eqs. 4 and 5) match well with the numerical solution of the wave dispersion equation. However, at high Ohnesorge and Weber numbers typical of Diesel engine operations, the discrepancy between correlations and numerical solution increased with Weber number as shown in Fig. 2a. These correlations were improved to obtain better fits to the numerical solution. However, the effect on global spray characteristics such as penetration was not pronounced as shown in Fig. 2b.

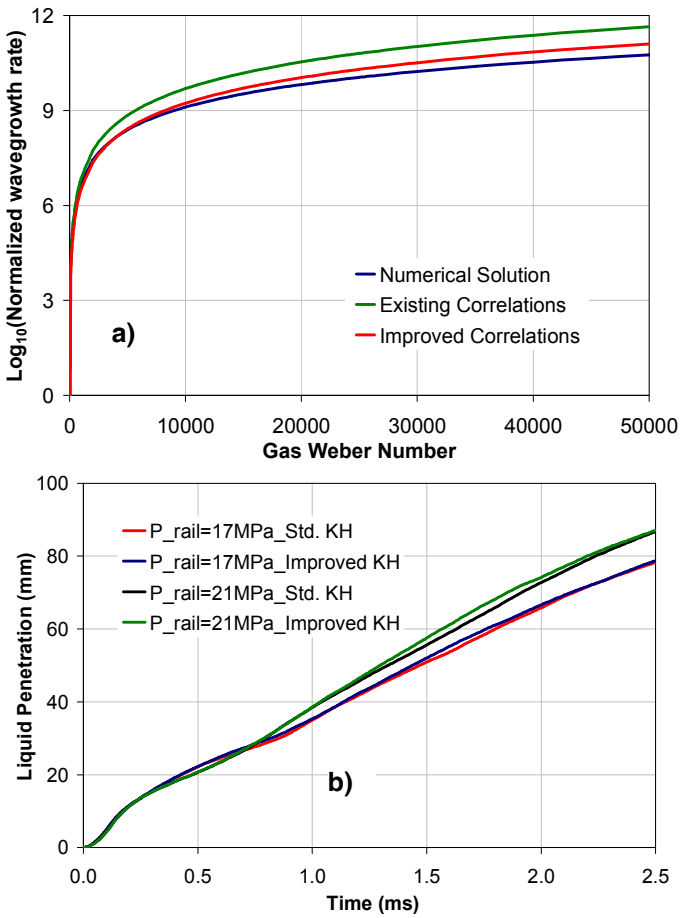

Figure 2: (a) Log normalized wave growth rate vs. gas Weber number for the numerical solution to the dispersion equation and correlations (b) Performance of the improved KH model against the standard KH for different rail pressure cases described in Table 1.

PRIMARY BREAKUP MODEL

As mentioned in the previous sections, primary breakup of the fuel spray in the region very close to the injector nozzle is influenced by cavitation and turbulence generated inside the nozzle as well as aerodynamic interactions between the liquid fuel and ambient gas outside. In this section, a brief overview of the improved primary breakup model that incorporates these effects is described.

TURBULENCE INDUCED BREAKUP MODEL: According to the Huh and Gosman model [10] the turbulent fluctuations in the jet are responsible for the initial perturbations on the jet surface. These waves grow according to KH instabilities until they breakup from the surface. The relevant length and timescales for turbulence induced breakup can be calculated as follows at any instant for any parcel:

$$L_T(t) = C_\mu \left(K(t)^{1.5} \big/ \varepsilon(t) \right) \tag{8}$$

$$\tau_T(t) = C_\mu \left(K(t) \big/ \varepsilon(t) \right) \tag{9}$$

Assuming isotropic turbulence for the liquid phase and neglecting the diffusion, convection, and production terms in the $k-\varepsilon$ equation, the decay of turbulent kinetic energy for a parcel was estimated as:

$$K(t) = \left\{ \frac{(K_0)^{C_\varepsilon}}{K_0\left(1 + C_\mu - C_\mu C_\varepsilon\right) + \varepsilon_0 t\left(C_\varepsilon - 1\right)} \right\}^{1/(1-C_\varepsilon)} \tag{10}$$

$$\varepsilon(t) = \varepsilon_0 \left\{ \frac{K(t)}{K_0} \right\}^{C_\varepsilon} \tag{11}$$

where K_0 and ε_0 are the initial values at the nozzle exit at start of injection (SOI) , determined from nozzle flow simulations [14]. The traditional approach is to determine these values using a simple force balance, not accounting for the decay in turbulence levels [10]. The approach used in this study thus provides a more accurate representation of turbulence quantities at any time step.

CAVITATION INDUCED BREAKUP MODEL: Cavitation patterns generated inside the injector nozzle can reach the nozzle exit, implosion of which enhances jet atomization. According to Bianchi and Pelloni [11] and Arcoumanis and Gavaises [8], the characteristic time-scale of cavitation (τ_{CAV}) is assumed to be the smaller of a bubble collapse time and a bubble burst time:

$$\tau_{CAV} = \min\left(\tau_{Collapse} : \tau_{Burst}\right). \tag{12}$$

The bubble collapse time is calculated from Rayleigh Plesset theory [28] as:

$$\tau_{Collapse} = 0.9145 R_{CAV} \sqrt{\frac{\rho_l}{p_v}} \tag{13}$$

where R_{CAV} is the effective radius of an equivalent bubble from the nozzle calculated as:

$$R_{CAV} = r_{hole}\sqrt{(1 - C_a)} \tag{14}$$

The area reduction coefficient (C_a) is calculated from the nozzle flow simulations [14] and r_{th} is the exit radius of the nozzle orifice. The average time required for a cavitation bubble to reach the periphery of the jet can be estimated as:

$$\tau_{Burst} = \frac{r_{hole} - R_{CAV}}{u'_{turb}} \tag{15}$$

where $u'_{turb} = \sqrt{\frac{2K(t)}{3}}$ is obtained from inner nozzle flow simulations. The length scale for the cavitation induced breakup is calculated as:

$$L_{CAV} = R_{CAV}\,. \tag{16}$$

AERODYNAMICALLY INDUCED BREAKUP MODEL: The improved KH model described in the previous

section is used to calculate the instantaneous length and time scales for every parcel:

$$L_{KH} = r - r_{KH} \tag{17}$$

$$\tau_{KH} = \frac{3.276 B_1 r}{\Omega_{KH} \Lambda_{KH}} \tag{18}$$

The ratio of length and time scales for each process is calculated. As seen from Eqs. 2 and 20, rate of decrease in droplet radius scales with the ratio of length to time scale. Thus the largest ratio determines the dominant breakup process.

$$\frac{L_A}{\tau_A} = \max\left\{\frac{L_{KH}(t)}{\tau_{KH}(t)}; \frac{L_{CAV}}{\tau_{CAV}}; \frac{L_T(t)}{\tau_T(t)}\right\} \tag{19}$$

If aerodynamic interactions are dominant then the breakup law from Eq. 2 is used for primary breakup of the parcel. However, if cavitation or turbulence processes dominate then the following breakup law is used:

$$\frac{dr}{dt} = -C_{T,CAV} \frac{L_A}{\tau_A} \tag{20}$$

A value of 0.025 is used for $C_{T,CAV}$. Child parcels are subjected to aerodynamic breakup only whereas parent parcels are subject to primary breakup

The inner nozzle flow simulations provided the necessary boundary conditions for the primary breakup model in terms of TKE, TDR, and extent of cavitation [14] at the nozzle exit. Quasi-steady state values at full needle lift position were: TKE=5072 m^2/s^2, TDR=5.8 E+9 m^2/s^3 with 4% vapor fraction at nozzle exit. In case nozzle flow modeling/measurements were not feasible, analytical expressions were used [11] to calculate TKE and TDR:

$$K_0 = \frac{U_{inj}^2}{8\left(L/D\right)}\left\{\frac{1}{C_d^2} - K_C - \left(1 - S^2\right)\right\} \tag{21}$$

$$\varepsilon_0 = K_\varepsilon \frac{U_{inj}^3}{2L}\left\{\frac{1}{C_d^2} - K_C - \left(1 - S^2\right)\right\} \tag{22}$$

However, the extent of cavitation in the absence of nozzle flow modeling could not be established. The model constants used are [11]: K_C=0.45, K_ε=0.27, S=0.01. Clearly, a drawback of the model is that nozzle flow conditions for turbulence and cavitation parameters are required as boundary conditions.

RESULTS AND DISCUSSION

NON-EVAPORATIING SPRAYS

Figure 3 presents the predicted and measured spray penetration for the two non-evaporating spray cases listed in Table 1. The injection pressure was calculated from the rail pressure using a pressure amplification ratio of 6.6. The penetration data was available up to 0.2ms from the SOI. In simulations the liquid penetration at a particular instant is calculated by locating the axial position that encompasses 97% of the total injected mass until that time. For both rail pressures, a slow penetration region up to 0.08 ms is followed by a faster penetration region (where penetration linearly scales with time) up to 0.2ms. There is good agreement between simulations and experiments for both rail pressures. An important observation is that the higher rail pressure case shows lower penetration speeds than the lower rail pressure case in both experiments and simulations. This is unexpected, since higher injection pressure yields faster penetration [29]. As noted earlier, the ROI for the early transition region is based on the x-ray data. As discussed by Ramirez et al. [21], the x-ray data indicated a slower pressure build-up in the injector for the 21 MPa rail pressure case compared to that for the 17 MPa case. Consequently, the 21 MPa rail pressure case yields lower injection rate and thus lower spray penetration in the region close to the nozzle. Thus, in this region very close to the nozzle, only the upstream conditions affect spray penetration rather than the details of the spray models.

Figure 3 also presents the effect of ROI on spray penetration for the two rail pressures. While, the ROI from x-ray data was limited to 0.18ms after SOI, the Bosch rate meter provided ROI during the entire injection event, which was 3.4ms and 3.7ms for the 21MPa and 17MPa rail pressures, respectively. Using ROI from the rate meter (cf. Fig. 1) leads to gross underprediction of spray penetration while that from the x-ray data shows good agreement. This again reiterates the fact that in the region close to the nozzle, the upstream conditions affect spray penetration rather than the details of the spray models. Hence, accurate determination of rate of injection profile is critical for validating the spray models. ROI also forms an important boundary condition for engine and spray simulations. Clearly, in the region close to the nozzle and during the initial stages of spray development the standard Bosch rate meter is not able to capture the spray dynamics. More sophisticated tools, such as x-ray radiography, are required for determining the ROI throughout the duration of injection.

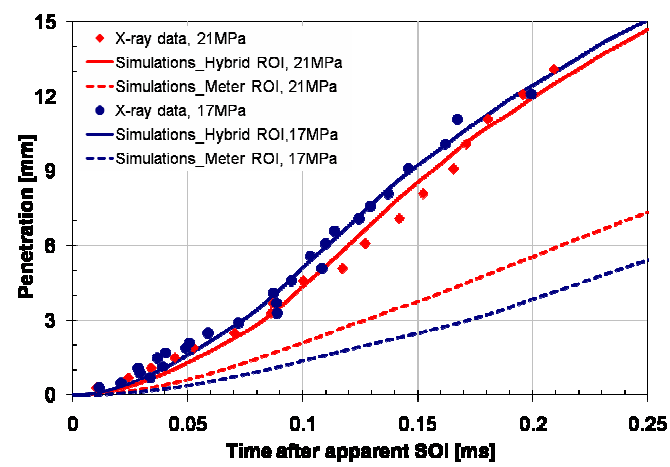

Figure 3: Validation of the primary breakup model against non-evaporating spray penetration data (cf. Table 1) for oil rail pressures of 17 and 21 MPa, at 30 bar

back pressure. Effect of ROI on spray penetration is also shown.

Figure 4 presents spray penetration versus time for different spray models. It should be noted that a competition between KH and RT models was still used as the secondary breakup mechanism. The difference between simulations lies with the choice of their primary breakup mechanism. The standard KH model is used as the base model for comparisons. The enhanced primary breakup model is demarcated as the "new model". The new model is also tested without turbulence and cavitation models. It is seen that the spray penetration decreases significantly with inclusion of turbulence and cavitation induced breakup. Turbulence from the nozzle orifice is seen to have a greater impact on spray penetration than cavitation. This is not surprising since the amount of cavitation generated from the nozzle was observed to be rather low [14]. Also interesting to note is that the new primary breakup model affects spray penetration during the later stages i.e., after 0.65ms. This is due to the fact that the primary breakup mechanism enhances atomization thus decreasing the parent parcel sizes (SMD) and greater number of child parcels is formed. However, initial penetration solely depends on upstream conditions (ROI). Hence, these comparatively smaller parent and child parcels penetrate less at a later stage.

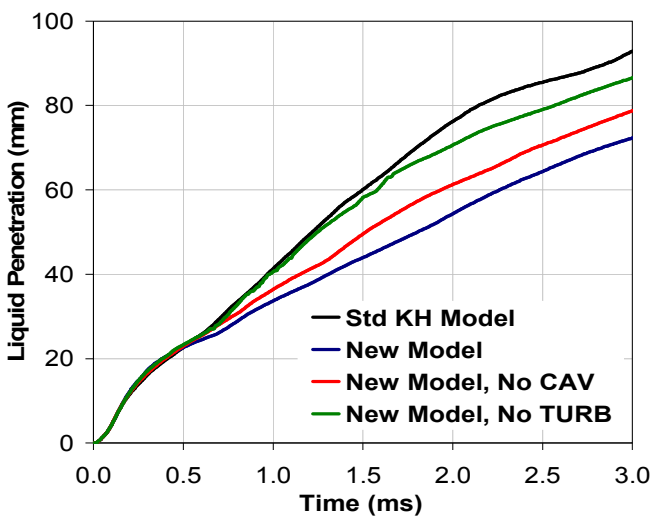

Figure 4: Effect of different spray models on spray penetration for 21MPa rail pressure case.

Figure 5 presents X-ray data and comparison between the standard KH model and new primary breakup model in terms of transverse distributions of projected density 0.99 ms after SOI for both rail pressures. The projected mass density profiles exhibit Gaussian distribution for both the measurements and simulations at 2.483mm from the nozzle tip (cf. Fig. 5a). In general it is seen that the standard KH model over-predicts mass density and underpredicts spray dispersion. With the new primary breakup model, results improve both in terms of peak values and spray dispersion for both rail pressures. Since the new primary breakup model predicts faster breakup than the standard model, more child droplets are produced which spread more thus improving spray dispersion. At 7.083mm from nozzle tip (cf. Fig. 5b) experiments predict higher spray dispersion. The new primary breakup model does a better job in predicting this increased spray dispersion at both rail pressures. In general it is seen that the new breakup model agrees closer to experimental data.

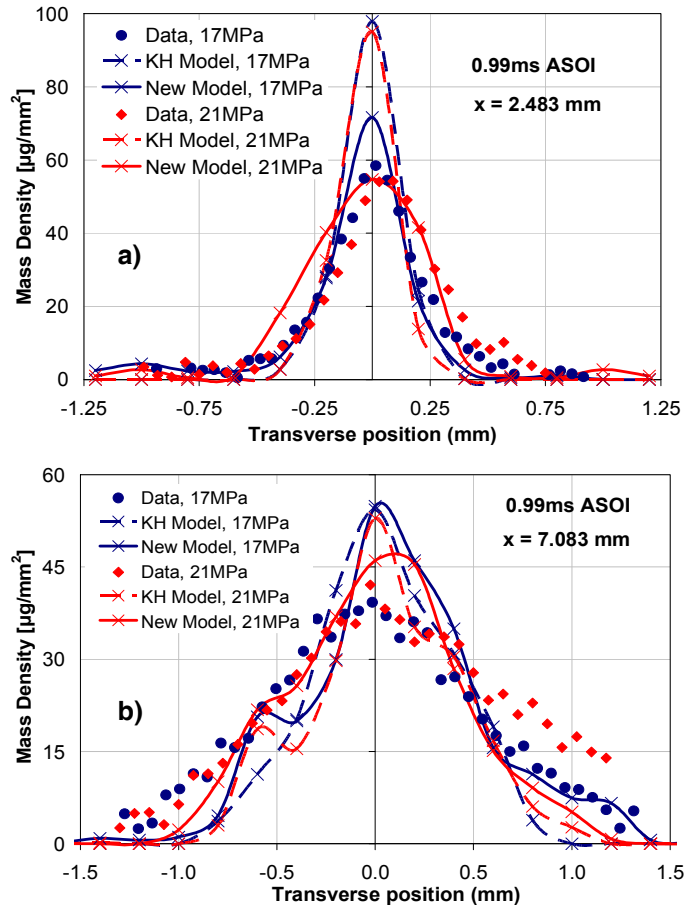

Figure 5: Comparison of standard KH model and new primary breakup model against x-ray data (cf. Table 1) obtained for transverse distributions of projected density for two rail pressure cases at (a) 2.483 mm and (b) 7.083mm from the nozzle tip 0.99ms after SOI.

Figure 6 presents further validation of the primary breakup model. In Fig. 6a the effect of moving away from the nozzle tip on spray dispersion is observed for 21 MPa rail pressure case. X-ray data shows that moving away from the nozzle tip, the spray spreads more and peak value decreases. Simulations capture this fairly well. At 0.283mm though the peak value is slightly under predicted by simulations. Fig. 6b presents mass density at different times after SOI for a fixed axial location of 2.483mm. X-ray data predicts similar spray dispersion at all times with the peak values decreasing slightly with time. Simulations show higher sensitivity towards mass density at different times after SOI. Peak value trends are captured very well by simulations. In general, small differences between experimental data and the new primary breakup model are observed. This could be an artifact of uncertainty associated with the ROI.

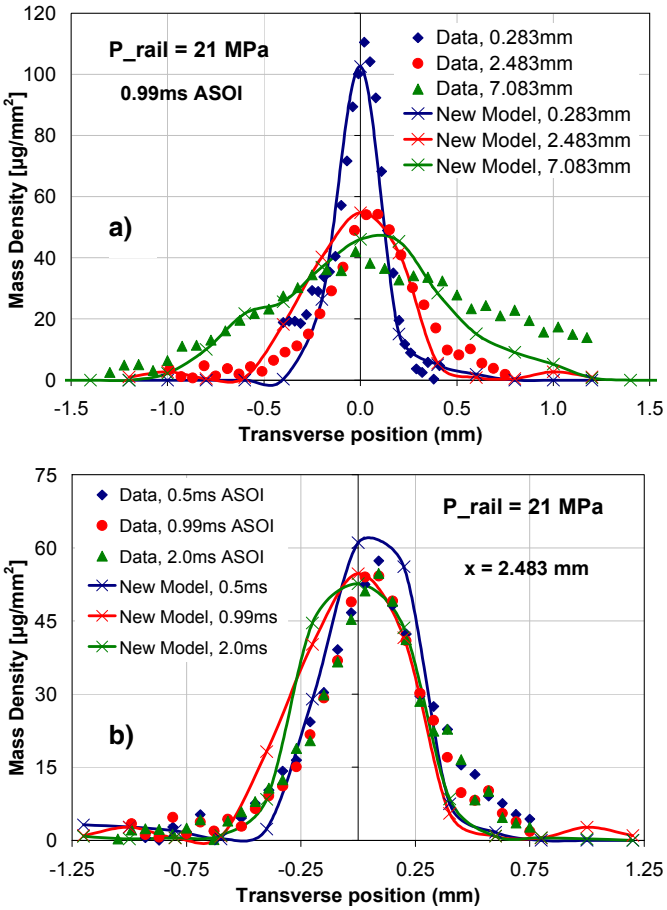

Figure 6: Validation of the new primary breakup model against x-ray data (cf. Table 1) obtained for transverse distributions of projected density (a) at 0.99ms after SOI for different distances from nozzle tip, (b) at 2.438mm from the nozzle tip for different times after SOI for 21 MPa rail pressure case.

Integrating the mass distribution (cf. Fig. 6) in the transverse direction yields the transverse integrated mass (TIM) at a given time and axial location [21]. TIM gives a perception of the amount of mass per unit length in the spray and hence its variation with axial distance is of fundamental importance. Figure 7 presents the computed TIM based on the x-ray data and simulations, along the axial location at 0.99ms after SOI for both rail pressure cases. TIM was seen to continuously increase with axial position [30] and simulations captured this trend very well for both the rail pressures. Monotonic increase of TIM with axial position is due to the fact that the spray axial velocity decreases due to ambient drag, hence in order to conserve spray momentum at every axial location, the TIM must increase. The standard KH model underpredicts TIM after 2.5mm from the nozzle tip. New model performs a much better job in predicting TIM especially upto 8mm. Thereafter the new model is seen to over predict. Differences between data and simulations may be attributed to different methodology of TIM calculations in simulations and experiments.

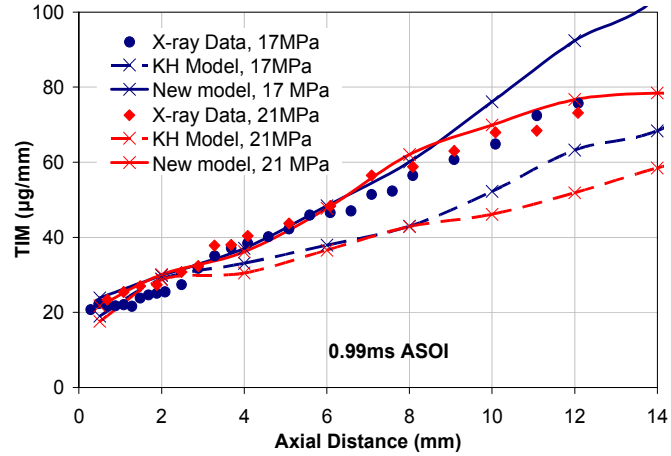

Figure 7: Comparison of standard KH model and new primary breakup model against x-ray data (cf. Table 1) for Transverse Integrated Mass (TIM) vs. axial position at 0.99 ms after SOI for 17 and 21 MPa oil rail pressures.

Figure 8a presents the normalized axial velocity versus axial position based on the x-ray data and simulations at 0.99 ms after SOI for both rail pressure cases. X-ray data was available only for the 17MPa case while from simulations normalized spray axial velocity could be computed for both rail pressures. In simulations, the normalized spray axial velocity at a given instant in time was computed by averaging the axial velocity on mass basis, and normalizing it by its corresponding value at the nozzle exit. While there is notable difference in the near nozzle region (x < 3mm), there is fairly good agreement between predictions and measurements further downstream. The reason for differences in the near nozzle region needs to be further investigated. It is important to note that while the decay of spray velocity in the downstream direction is expected, both the measurements and simulations indicate a rather rapid decrease, with the normalized velocity decreasing to half its initial value at 5mm from the nozzle tip. This indicates that spray penetration and thus interaction with unburnt air which promotes fuel-air mixing would be significantly slower beyond this near nozzle region. The standard KH model is seen to over predict normalized spray velocity while the new model matches very well with the data.

Figure 8b presents the effect of time evolution on normalized spray axial velocity for the 21MPa rail pressure case at 0.99ms after SOI. Initially (0.5ms after SOI) the normalized spray velocity decreases very rapidly reaching half its value within 3mm from the nozzle tip. At 0.99ms the normalized spray velocity seems to reach a steady state value since the results do not change appreciably at 2ms after SOI. It should be noted that the results for only 21MPa rail pressure case are shown on many instances, however, the results for 17MPa rail pressure case was also qualitatively similar.

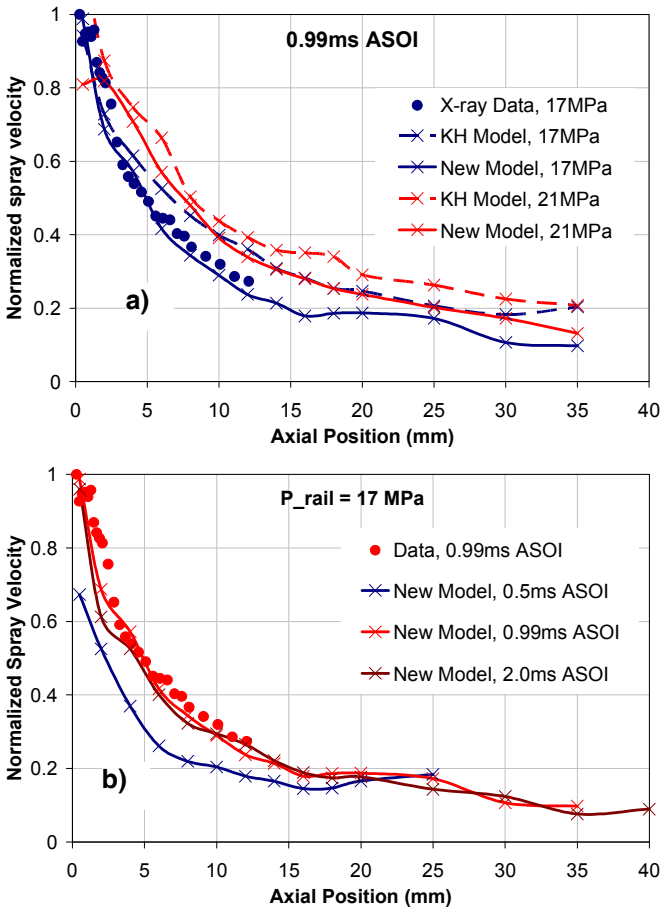

Figure 8: (a) Comparison of standard KH model and new primary breakup model against x-ray data (cf. Table 1) for normalized spray axial velocity vs. axial position at 0.99 ms after SOI for 17 and 21MPa oil rail pressures. (b) Effect of time evolution on normalized spray velocity for the 17MPa rail pressure case.

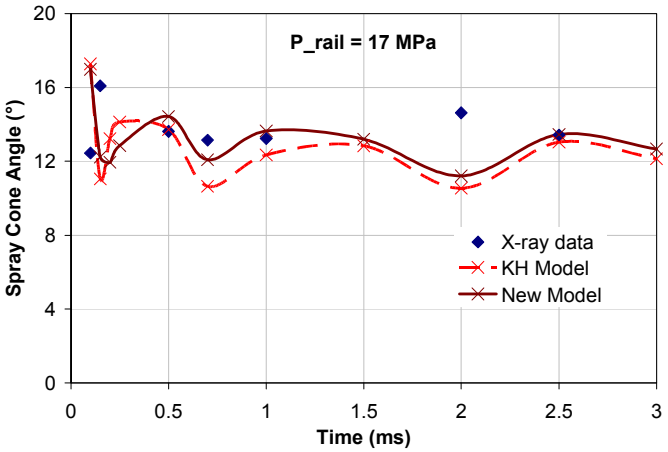

Figure 9: Comparison of standard KH model and new primary breakup model against measured (cf. Table 1) spray cone-angle data for 17MPa rail pressure case.

Figure 9 presents a comparison of the new model and x-ray data for spray cone angle as a function of time for the 17MPa rail pressure case. In experiments spray penetration was defined at a location of 4mm from the nozzle tip when the mass density dropped to 20% of the peak value. In simulations the spray cone angle was calculated at 4mm based on the extent of spreading of droplets. It is seen that in general the new primary breakup model predicts higher spray cone angle which is consistent with earlier results (cf. Fig. 5) where spreading was observed to be greater for the new model.

Effect of Nozzle Orifice Geometry

The effects of nozzle conicity on spray tip penetration are analyzed in this section. The nozzle conicity is represented in terms of K_{factor} as:

$$K_{factor} = \frac{(D_{in} - D_{out})}{10} \ \mu m \qquad (23)$$

Figure 10 shows the effects of nozzle conicity on spray tip penetration at a rail pressure of 21 MPa. From cavitation simulations it was observed that the K_{factor}=0 case was cavitating with cavitation patterns reaching the nozzle exit. Consequently, the exit density was about 4% lower than the liquid density. With decrease in exit area (or increase in K_{factor}) the average exit velocity increased by 10% for K_{factor}=2 case. These changes were incorporated into the original ROI profile reported by Ramírez et al. [21]. The new ROI profiles calculated were lower in magnitude due to the decrease in exit area owing to increase in K_{factor} , i.e., the mass injected was lower at higher K_{factor} values. This observation is consistent with the findings of Benajes et al. [31].

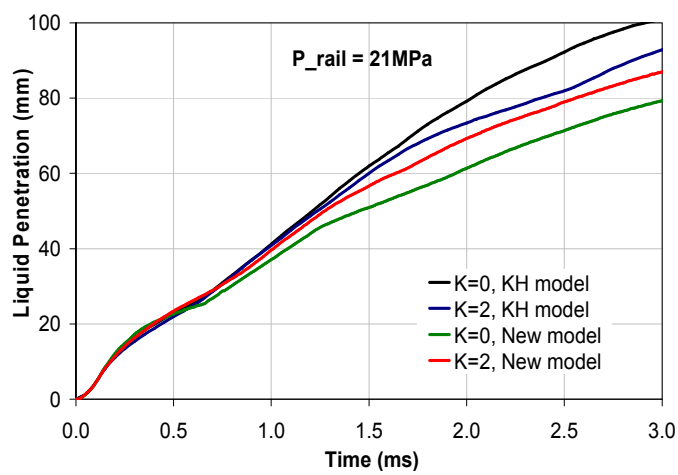

Figure 10: Comparison of standard KH model and new model in predicting the effect of nozzle orifice conicity on spray penetration versus time for 21 MPa rail pressure case.

The standard KH model predicts a decrease in spray tip penetration with increase in K_{factor}. This is in disagreement with the experimental trends observed [15,16]. The new primary breakup model captures the experimental trend accurately, i.e., with increase in K_{factor} the spray tip penetration increases. It is well established that imploding cavitation patterns and turbulence patterns from the nozzle destabilize the jet thus promoting faster atomization which leads to lower spray penetration. Standard primary breakup models like KH are aerodynamics based and hence do not capture the

nozzle flow effects. Hence their disagreement with this experimental trend is not surprising.

Figure 11 presents the effect of K_{factor} (K) on spray mass density, TIM, and normalized spray axial velocity. Note that a K=2 orifice represents an exit diameter of 149μm as compared to 169μm for K=0. From Fig. 11a it is seen that the spray spreading decreases with increase in K_{factor} at simultaneous axial distances from nozzle orifice while peak values increase at both axial locations. This is expected since the exit diameter for K=2 is about 12% lower than that of K=0. Also it should be noted that the exit velocity for K=0 was about 10% lower than that of K=2. A spray with lower injection velocity for a fixed back pressure is expected to spread more. Thus decreased spray spreading at higher K_{factor} values can be understood. From Fig. 11b TIM is seen to be higher for K=0 which is due to the fact that mass injected is also higher for the cylindrical nozzle (K=0). Normalized spray velocity was seen to decay at a faster rate for K=0 than K=2. For the cylindrical nozzle the spray spreading was higher thus interaction with the gas was greater which resulted in faster momentum exchange. After an axial distance of 8mm the decay in axial spray velocity is almost similar for both K_{factor} cases. The inverse correlation between TIM and normalized spray velocity observed here is consistent with previous experimental studies of our group [21].

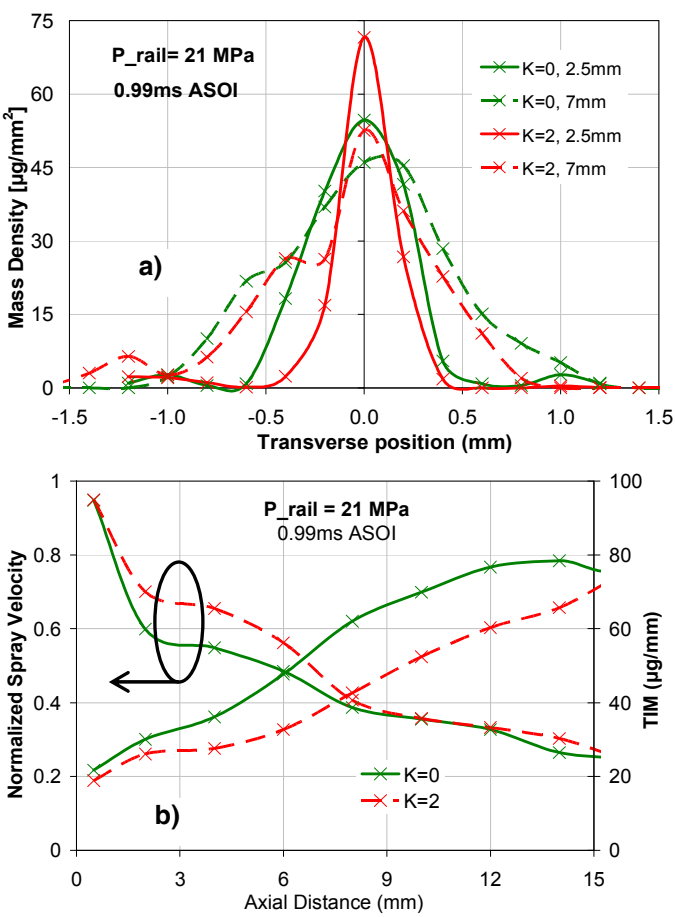

Figure 11: Effect of nozzle orifice conicity on (a) spray mass density, (b) TIM and normalized axial spray velocity for 21MPa rail pressure case 0.99ms after SOI.

After performing detailed validation of the new primary breakup model under non-evaporating conditions we present validation under evaporating conditions.

EVAPORATIING SPRAYS

This section presents assessment of spray models under evaporating conditions typical of part load diesel engine operation.

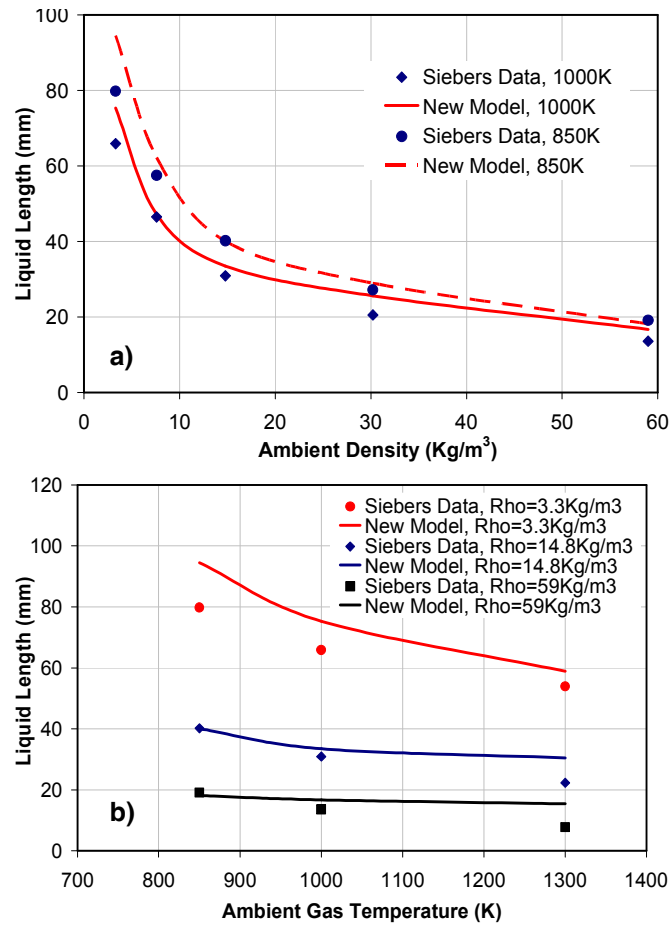

Figure 12: Measured and predicted liquid lengths plotted (a) versus ambient gas density for two different ambient gas temperatures, and (b) versus ambient gas temperature for four different ambient gas densities.

Figure 12 plots the effects of ambient gas density and temperature on liquid length for evaporating sprays. The orifice diameter, injection pressure, and fuel temperature were 246 μm, 142 MPa and 438 K, respectively in the experiments [19]. Note that under evaporating conditions, the liquid length is defined as the maximum liquid penetration distance. It represents an important spray characteristic since over penetration can result in impingement on combustion chamber walls and pistons, with associated increase in engine raw emissions, while under penetration results in poor air utilization. As expected, with increase in ambient gas density, the drag on droplet parcels increases, and consequently, the liquid length decreases. This trend is well captured by simulations (cf. Fig. 12a). Similarly, an increase in ambient temperature at a fixed density causes a decrease in liquid length (cf. Fig. 12b). This can

be attributed to the increased vaporization rate, which decreases the overall droplet size, and thus the liquid length. This trend is fairly well captured by simulations for the two low ambient density cases (ρ_a =3.3 kg/m^3 and 7.6 kg/m^3). However at higher densities (ρ_a =14.8 kg/m^3 and 59 kg/m^3), the predicted liquid lengths are relatively insensitive to changes in ambient gas temperature.

Figure 13 plots the measured and predicted vapor penetration profiles at four different ambient gas densities. The orifice diameter, injection pressure, ambient gas temperature, and fuel temperature were 246μm, 142MPa, 1000K, and 438K, respectively [19]. In simulations the liquid penetration at a particular instant is calculated by locating the axial position which encompasses 97% of the injected fuel mass. Once liquid length is established, vapor penetration defines the extent of fuel penetration. For all the four cases, there is good agreement from 0.4ms to 1.6ms. In general, the agreement is good especially at higher ambient densities. However, some differences during the later stages of injection are seen. The differences during early part of injection are attributed to uncertainties with rate of injection profiles. The overall match was better than that observed by previous studies (e.g., [32]) for the range of conditions simulated.

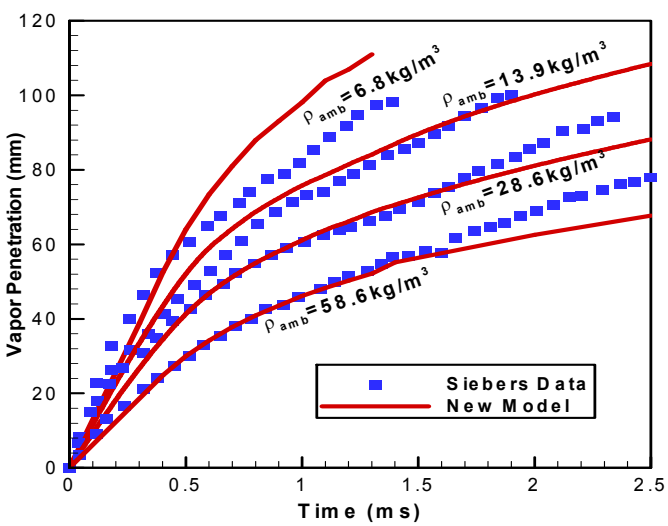

Figure 13: Measured and predicted vapor penetration versus time for three different ambient gas densities. The orifice diameter, injection pressure, ambient temperature, and fuel temperature were 246μm, 142MPa, 1000K and 438K respectively.

Figure 14 presents comparison between simulations and measurements in terms of the liquid length as a function of various parameters at different ambient conditions. With increase in fuel temperature, the liquid length decreases (cf. Fig. 14a). This is expected since as the fuel temperature increases evaporation rate is enhanced and less energy is required for evaporation. In addition, the effect of fuel temperature is more pronounced at lower ambient temperature and density. Simulations capture these trends very well. At lower ambient temperature (700K) and higher fuel injection temperature there are small differences between the experimental and predicted results. Figure 14b presents experimental and simulated results for the effects of orifice diameter on liquid length. Under all experimental conditions liquid length is seen to vary linearly with orifice diameter. This is an important result for designing since with a smaller orifice; smaller liquid lengths can be achieved thus decreasing the chances of piston and wall impingement. Again these trends are successfully captured by the simulations. It should be noted here that all the simulations were run with the same set of new model, KH, and RT constants.

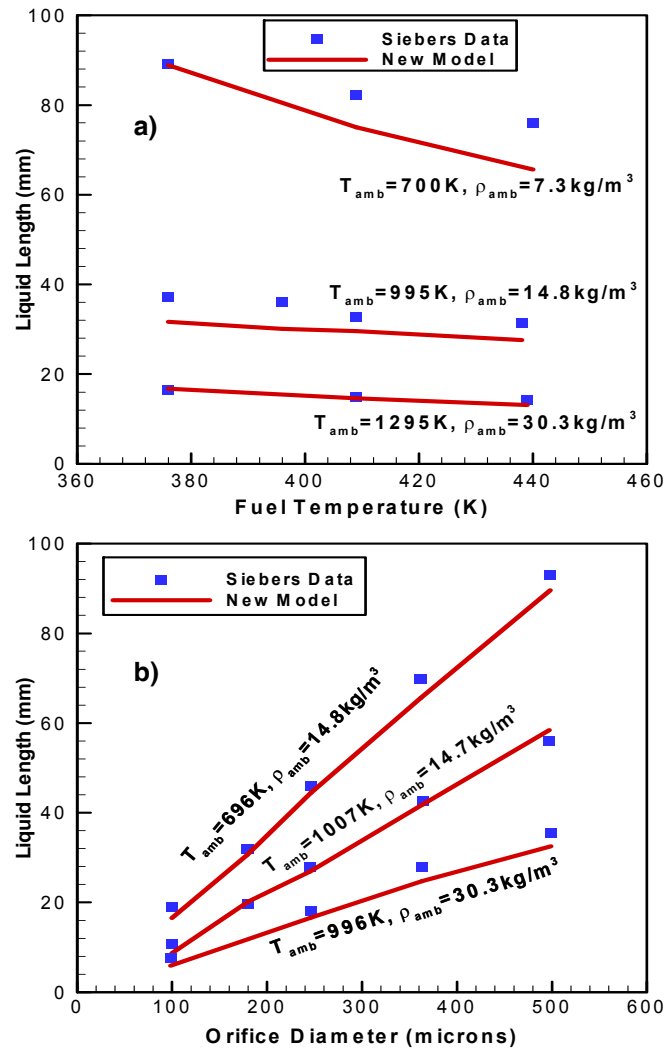

Figure 14: Measured and predicted liquid length versus (a) Injected fuel temperature and (b) Orifice exit diameter for three different ambient gas conditions. The injection pressure was 142MPa.

CONCLUSIONS

Following up on our previous work [13], we have developed and implemented an enhanced primary breakup model capturing the effects of cavitation and

turbulence in an engine modeling software, CONVERGE. Some important conclusions are:

- Rate of injection profile is seen to have a significant impact on spray penetration especially near the nozzle tip and during early stages of injection. Accurate prediction of near nozzle penetration characteristics was possible only by using the ROI from x-ray data.
- Spray dispersion was better captured under all conditions investigated by the new primary breakup model than the standard KH model.
- Microscopic spray properties like TIM, normalized axial velocity, and near field spray cone angle matched well with the experimental data available. In general the new primary breakup model performs better in terms of predicting non-evaporating spray characteristics.
- Experimentally observed trends with changing nozzle K_{factor} could not be captured by the standard KH models. The new primary breakup model is able capture those experimental trends. A cylindrical nozzle is seen to spread more than a conical nozzle.
- Under evaporating conditions liquid length and liquid penetration matched reasonably well with experimental data for all conditions simulated.

The new spray breakup model provides a scope for dynamic coupling between the nozzle flow and spray simulations since the effect of turbulence and cavitation generated inside the nozzle orifice can now be captured.

Following detailed validation under non-evaporating and non-combusting evaporating spray conditions, extensive comparisons [33] were made to measurements of liquid length and flame lift-off by Siebers and Higgins [34]. Effect of nozzle orifice diameter, injection pressure, ambient gas temperature, and ambient gas density on spray and combustion processes was studied. In general, the predicted flame lift-off and liquid length trends and magnitudes with the new model were in excellent agreement with available data in literature. Under certain conditions, this new primary breakup model was seen to perform better than the aerodynamically induced KH breakup model in predicting flame lift-off lengths [33]. Future efforts will focus on validating this new model against engine data which will be obtained from Argonne National Laboratory.

ACKNOWLEDGMENTS

This work is supported by the U.S. Department of Energy Office of Vehicle Technology under the management of Gurpreet Singh. The experiments were performed at the 1-BM beam-line of the APS. Use of the APS is supported by the U.S. Dept. of Energy under contract DE-AC02-06CH11357.

The submitted manuscript has been created by UChicago Argonne, LLC, Operator of Argonne National Laboratory ("Argonne"). Argonne, a U.S. Department of Energy Office of Science laboratory, is operated under Contract No. DE-AC02-06CH11357. The U.S. Government retains for itself, and others acting on its behalf, a paid-up nonexclusive, irrevocable worldwide license in said article to reproduce, prepare derivative works, distribute copies to the public, and perform publicly and display publicly, by or on behalf of the Government.

REFERENCES

1. Y. Yue, C.F. Powell, R. Poola, J. Wang, and J.K. Schaller (2001). Quantitative measurements of diesel fuel spray characteristics in the near-nozzle region using x-ray absorption. *Atomization and Sprays*, vol. 11, pp. 471–490.
2. R.D. Reitz, and R. Diwakar, Structure of high pressure fuel sprays, SAE Paper 870598, 1987.
3. M.A. Patterson, and R.D. Reitz, Modeling the effects of fuel spray characteristics on diesel engine combustion and emissions, SAE Paper 980131, 1998.
4. R.D. Reitz (1987). Modeling atomization processes in high-pressure vaporizing sprays. *Atomization Spray Technology*, vol. 3, pp. 309-337.
5. P.J. O'Rourke, and A.A. Amsden, The TAB method for numerical calculation of spray droplet breakup, SAE Paper 872086, 1987.
6. F.X. Tanner, Liquid jet atomization and droplet breakup modeling of non-evaporating diesel fuel sprays, SAE Paper 970050, 1997.
7. F.X. Tanner, A cascade atomization and drop breakup model for the simulation of high-pressure liquid jets, SAE Paper 2003-01-1044, 2003.
8. C. Arcoumanis, and M. Gavaises (1998). Linking nozzle flow with spray characteristics in a diesel fuel injection system. *Atomization and Sprays*, vol. 8, pp: 307-347, 1998.
9. E. Giannadakis, Modeling of Cavitation in Automotive Fuel Injector Nozzles. PhD thesis, Imperial College, June, 2005.
10. K.Y. Huh, and A.D. Gosman, A phenomenological model of diesel spray atomization, *Proceedings of the international conference of multi-phase flows*, 1991.
11. G.M. Bianchi, and P. Pelloni, Modeling the diesel fuel spray breakup by using a hybrid model, SAE Paper 1999-01-0226, 1999.
12. E.V. Berg, W. Edelbauer, A. Alajbegovic, R. Tatschl, M. Volmajer, B. Kegl, and L.C. Ganippa (2005). Coupled simulations of nozzle flow, primary fuel jet breakup, and spray formation, *ASME Journal of engineering for gas turbines and power*, vol. 127, pp: 897-908.
13. S. Som, and S.K. Aggarwal, A Numerical investigation of Non-Evaporating and Evaporating Diesel Sprays, ASME Paper IMECE2008-68441.
14. S. Som, S.K. Aggarwal, E.M. El-Hannouny, and D.E. Longman, Investigation of nozzle flow and cavitation

characteristics in a diesel injector, submitted to *ASME Journal of Gas Turbine and Power*, 2008.
15. F. Payri, V. Bermudez, R. Payri, and F.J. Salvador (2004). The influence of cavitation on the internal flow and the spray characteristics in diesel injection nozzles, vol. 83, pp. 419-431, 2004.
16. M. Blessing, G. Konig, C. Kruger, U. Michels, and V. Schwarz, Analysis of flow and cavitation phenomena in diesel injection nozzle and its effects on spray and mixture formation, SAE Paper 2003-01-1358 , 2003.
17. P.K. Senecal, E. Pomraning, K.J. Richards, T. Yang, M.Z. Dai, R.M. McDavid, M.A. Patterson, S. Hou, and T. Shethaji, A new parallel cut-cell Cartesian CFD code for rapid grid generation applied to in-cylinder diesel engine simulations, SAE Paper 2007-01-0159, 2007.
18. K.J. Richards, P.K. Senecal, E. Pomraning, CONVERGE™ (Version 1.2) Manual, Convergent Science Inc. (2008).
19. D.L. Siebers, Liquid-phase fuel penetration in diesel sprays, SAE Paper 980809, 1998.
20. J.D. Naber, and D.L. Siebers, Effects of gas density and vaporization on penetration and dispersion of diesel sprays, SAE Paper 960034, 1996.
21. A.I. Ramírez, S. Som, S.K. Aggarwal, A.L. Kastengren, E.M. El-Hannouny, D.E. Longman, and C.F. Powell, Quantitative measurement of diesel fule spray characteristics in the near-nozzle region of a heavy duty multi-hole injector, *21st ILASS Americas*, 2008.
22. J. Wang (2005). X-ray vision of fuel sprays, *Journal of Synchrotron Radiation*, vol. 12, pp. 197-207.
23. C.F. Powell, Y. Yue, R. Poola, J. Wang, M.C. Lai, and J. Schaller, X-ray measurements of high pressure diesel sprays, SAE Paper 2001-01-0531, 2001.
24. D.P. Schmidt, and C.J. Rutland (2000). A new droplet collision algorithm, *Journal of Computational Physics*, vol. 164, pp. 62-80.
25. A.A. Amsden, P.J. O'Rourke, and T.D. Butler, KIVA-II: A computer program for chemically reactive flows with sprays, Los Alamos National Laboratory Report No. LA-11560-MS, 1989.
26. S.L. Post, and J. Abraham (2002). Modeling the outcome of drop-drop collisions in diesel sprays, *International Journal of Multiphase flow*, vol. 28, pp. 997-1019.
27. A.B. Liu, D.K. Mather, and R.D. Reitz, Modeling the effects of drop drag and breakup on fuel sprays, SAE Paper 930072, 1993.
28. E.C. Brennen, *Cavitation and Bubble Dynamics*, Oxford University Press, 1995.
29. R. Payri, F.J. Salvador, J. Gimeno and J. Morena, Macroscopic Behavior of Diesel Sprays in the Near-Nozzle Field, SAE Paper No. 2008-01-0929, 2008.
30. A.I. Ramirez, S. Som, S.K. Aggarwal, A.L. Kastengren, E.M. El-Hannouny, D.E. Longman, and C.F. Powell, Quantitative X-Ray Measurements of High-Pressure Fuel Sprays from a Production Heavy Duty Diesel Injector, Submitted to *Journal of Experiments in Fluids*, 2008.
31. J. Benajes, J.V. Pastor, R. Payri and A.H. Plazas (2204). Analysis of the influence of diesel nozzle geometry in the injection rate characteristic, *ASME Journal of Fluid Engineering*, vol. 126, pp. 63-71.
32. J.C. Beale, and R.D. Reitz (1999). Modeling spray atomization with the Kelvin-Helmholtz/ Rayleigh-Taylor hybrid model, *Atomization and Sprays*, vol. 9, pp. 623-650.
33 S. Som and S.K. Aggarwal, Modeling Diesel Spray Flame Lift-off using Detailed Chemistry and a New Primary Breakup Model, 47th AIAA Aerospace Sciences Meeting, AIAA-2009-0666 (2009).
34. D.L. Siebers, and B. Higgins, Flame lift-off on Direct-Injection Diesel Sprays under Quiescent Conditions, SAE Paper No. 2001-01-0530 (2001).

CONTACT

Sibendu Som is a graduate student at University of Illinois at Chicago. E-mail: ssom1@uic.edu

DEFINITIONS, ACRONYMS, ABBREVIATIONS

r_{KH}	radius of newly formed droplets
Λ_{KH}	wavelength of the KH wave
Ω_{KH}	maximum growth rate of the KH wave
B_0, B_1	KH model constants
r	radius of the parent droplet parcel
t	time
dt	time-step size
τ_{KH}	KH model breakup time
σ	Surface tension
ρ_g	Gas density
ρ_l	Liquid density
U_r	Relative velocity between the phases
ν_l	Liquid viscosity
$L_T(t)$	Length scale at any instant for turbulence induced primary breakup model
$\tau_T(t)$	Time scale at any instant for turbulence induced primary breakup model
TKE	Turbulent Kinetic Energy
TDR	Turbulent Dissipation Rate
SOI	Start of Injection
$K(t)$	Instantaneous TKE for a parcel
$\varepsilon(t)$	Instantaneous TDR for a parcel
C_μ, C_ε	$k-\varepsilon$ model constants

K_0, ε_0	Initial TKE, TDR for a parcel
L_{CAV}, τ_{CAV}	Characteristic length and time-scale due for cavitation induced primary breakup model
$\tau_{Collapse}$	Bubble collapse time-scale
τ_{Burst}	Bubble burst time-scale
p_v	Vapor pressure for fuel
r_{hole}	Exit radius of the orifice
u'_{turb}	Turbulent velocity
$C_{T,CAV}$	Model constant for primary breakup model
L_A, τ_A	Dominant length and time scales
U_{inj}	Injection Velocity
L/D	Ratio of length to the diameter of an orifice
$C_{T,CAV}$	Breakup law constant = 0.05
D_{in}, D_{out}	Inlet and outlet diameters of nozzle orifice
SOI	Start of injection
μ	Microns